Desalination and Water Treatment
www.deswater.com

doi: 10.5004/dwt.2019.23584

144 (2019) 355–369
March

Recovery of phosphate from wastewater using alumina nanotubes

Muhammad Naveed Afridi, Jinsil Lee, Jong-Oh Kim*

Department of Civil and Environmental Engineering, Hanyang University, 222 Wangsimni-ro, Seongdong-gu, Seoul 04763, Korea, Tel. +82-2-2220-0325; email: jk120@hanyang.ac.kr (J.-O. Kim), Tel. +82-2-2220-4703; emails: naveedafridi92@yahoo.com (M.N. Afridi), trutha2@naver.com (J. Lee)

Received 6 March 2018; Accepted 11 July 2018

ABSTRACT

Phosphorus is an essential nutrient for every plant and animal. Excess of phosphorus stimulates algal growth in water bodies, resulting in eutrophication of the surface water. In this work, self-organized hexagonal nanotubes were fabricated on the surface of aluminum foil via a two-step electrochemical anodization, and the adsorption performance of the alumina nanotubes (ANT) for phosphate removal from wastewater was evaluated. The morphology of the ANT film was characterized by field emission scanning electron microscopy, X-ray diffraction, energy dispersive X-ray spectroscopy, and Fourier transform infrared spectroscopy. The different parameters that affect the adsorption, such as the initial PO_4^{3-} concentration, pH, contact time, temperature, and coexisting anions, were investigated. The adsorption isotherm results illustrated that the Langmuir model was more suitable than the Freundlich model. Thermodynamic studies showed that the adsorption of phosphate was endothermic and spontaneous in nature. The adsorption capacity of ANT was more effective at acidic pH because of the increase in attractive forces between the phosphate anions and charges on the ANT surface. Kinetic modeling studies showed that the adsorption process obeyed the pseudo-second order. The adsorbed phosphate was successfully detached using NaOH. Thus, it was concluded that ANT is a highly efficient adsorbent material for phosphate recovery from wastewater.

Keywords: Anodization; Alumina nanotubes; Adsorption; Phosphate; Reusability

1. Introduction

Phosphorus is an essential nutrient for plants and animals, and its deficiency in the agricultural land can result in limited crop production. Therefore, phosphorus and its compounds are widely used as fertilizers in agriculture. It is also used as an ingredient for human food, detergents, polishes, and some specialty chemicals. However, its discharge into surface water bodies via agricultural runoff and wastewater contributes to eutrophication, leading to environmental problems in reservoirs and coastal areas [1–3]. Therefore, it is necessary to either remove or reduce the amount of phosphorus contained in wastewater to low concentrations to avoid eutrophication [4].

In recent years, different methods have been applied for the removal of phosphate from wastewater, including physical separation, chemical precipitation, and other biological processes [5–7]. The chemical precipitation method, while being effective, poses problems for sludge handling and disposal because of use of chemicals [8,9]. Biological methods for removing phosphate utilize phosphate-solubilizing fungi or activated microorganisms to adsorb phosphate and convert it into fertilizers [10]. However, the efficiency of these techniques is sensitive to fungal or microbial environments; therefore, it is difficult to remove phosphate at a steady rate [11]. Physical treatment methods to remove phosphate from wastewater such as reverse osmosis, ion exchange, electrodialysis, and adsorption appear to be much more promising than chemical treatment methods [12]. With the exception of adsorption, most of these physical methods have proven to be either too expensive or ineffective [13]. Adsorption is one of the most

* Corresponding author.

Presented at the 2017 International Environmental Engineering Conference & Annual Meeting of the Korean Society of Environmental Engineers (IEEC 2017), 15–17 November 2017, Jeju, Korea.

attractive and efficient physical methods of phosphate removal from wastewater with low phosphate concentration because of low recurring cost, simplicity in performance and operation, and production of less sludge volume [14,15].

Several adsorbents such as aluminum oxides, iron oxides, red mud, alum sludge, lanthanum oxide, mesoporous silicates, zirconium oxides, and hydroxides have attracted attention as useful materials for phosphate removal [6,14,16]. Although these adsorbents exhibit high phosphate removal efficiency, they suffer from limitations such as agglomeration, the loss of particles during adsorption, and the need for an additional separation technique for their recovery [17].

In recent years, electrochemical anodization has attracted considerable attention in wastewater treatment. Anodization is a useful method for modifying the surface of a metal substrate to obtain nanoporous or nanotubular structures [18,19]. In this process, when the surface of the metal is exposed to an oxygen-containing environment, it is immediately covered with a native oxide film. The oxide film can be subsequently used for fabricating ordered pore arrays [20]. This is a promising way to prepare large-area nanometer-sized structures, especially with high aspect ratios. For example, Al_2O_3 nanotube arrays (ANT) have been successfully synthesized by anodization. Nanotube arrays with tubular structures and large specific surface areas can be used as nanoreactors. In addition, they can be easily removed from the reaction system because of their large size. Therefore, ANT arrays may have wide applicability in wastewater treatment [20–22].

In this work, we fabricated self-organized hexagonal nanotubes on the surface of aluminum (Al) foil via a two-step electrochemical anodization method using oxalic acid as an electrolyte. Furthermore, we investigated the possibility of the utilization of ANT as an adsorbent for the recovery of phosphate (PO_4^{3-}) from synthetic wastewater. To the best of our knowledge, the recovery of phosphate from wastewater using ANT as an adsorbent has not been reported to date.

2. Materials and methods

2.1. Materials and chemicals

Al foil (5 × 4 cm^2 in size, purity 99.5%, thickness 0.25 mm) was purchased from Joil Aluminum Co., Ltd., Korea. Acetone, perchloric acid, oxalic acid, and KH_2PO_4 were obtained from Daejung Chemicals & Metal Co. Ltd., Korea. Ethanol was acquired from Samchun Pure Chemical Co. Ltd., Korea, and chromic acid was purchased from Sigma-Aldrich Korea Ltd, Korea. All chemicals and solvents were of analytical grade and used as received.

2.2. Synthesis of ANT

ANT was prepared using Al foil via two-step anodization as shown in supplementary material Table S1. Prior to anodization, Al foil was degreased with acetone by sonication for 15 min. Then, it was electropolished in a 1:4 (v/v%) mixture of $HClO_4$ and ethanol by applying a 10-V anodic potential for 3 min. The electropolished sample was washed with deionized (DI) water and dried with nitrogen gas to prevent the oxidation of Al foil. The electropolishing process resulted in a clear mirror-like Al foil. Subsequently, heat treatment (annealing) was conducted for 20 min at 500°C using an electric furnace (SF-03, SciLab Co., Korea). The first anodization step was conducted at different applied voltages (10–70 V) in 0.3M oxalic acid with a DC power supply (N6702A, Agilent Co., USA) for different time durations (1–8 h). The temperature of the electrolyte was maintained at 5°C using a circulator (HST-205WL, Hannaek Co., Korea). After the first anodization step, the sample was chemically etched with mixed acid (6 wt.% H_3PO_4 + 1.8 wt.% H_2CrO_4 aqueous solution) at 60°C for 4 h to remove the nonuniform and irregular oxide layer formed during the first anodization. The etched sample was then washed with DI water and dried using nitrogen gas. In the second anodization step, the sample was anodized at 30 V for different time durations (1–8 h) to obtain a highly oriented nanostructure and uniform ANT arrays.

2.3. Characterization

The surface morphology of the ANT was examined using field emission scanning electron microscopy (FE-SEM, Sigma, Carl Zeiss Co., Germany). The crystal structure was analyzed using X-ray diffraction (XRD, D8-Advance, Bruker-AXS Co., Germany). Elemental analysis and the chemical composition of the ANT were examined using energy-dispersive X-ray spectroscopy (EDX, Noran System 7, Thermo Fisher Scientific Co., USA). Surface functional groups were analyzed using Fourier transform infrared spectroscopy (FTIR, Spectrum Two, PerkinElmer, USA).

2.4. Adsorption of phosphate by ANT

Potassium dihydrogen phosphate (KH_2PO_4), used as a phosphate source, was dissolved in DI water to obtain the phosphate solution. Adsorption processes for single-factor experiments were conducted as follows: a piece (surface area: 20 cm^2) of ANT was added into a 50-mL conical tube with 20 mL of the phosphate solution (50 mg L^{-1}). The closed conical tubes were then placed in a rotator shaker (GTR-100, Green Tech Co., Korea) at room temperature for 4 h to achieve an equilibrium state. Phosphate concentration was determined by using the standard method 10127 with a high-range limit of 100 mg L^{-1} PO_4^{3-} using a UV-spectrophotometer (Hach, DR3900, USA).

In order to determine the maximum adsorption capacity of ANT, equilibrium batch tests were conducted as described above using various initial concentrations (10, 25, 50, 100, 200, 400, 700, 1,000, 1,500, 2,000, and 2,500 mg L^{-1}) at three different temperatures (10, 25, and 40°C) with pH adjusted to 5. It is well known that phosphate ions in strongly acidic or basic medium can cause dissolution of the aluminum oxide; therefore, it might be possible to damage the ANT. To avoid the risk of damaging the adsorbent, pH 5 was chosen for this study. The adsorption capacity of ANT for phosphate was determined using Eq. (1):

$$q_e = \frac{C_0 - C_e}{m} \times V \tag{1}$$

where q_e is the equilibrium adsorption capacity per unit weight of the adsorbent (mg g^{-1}); C_0 and C_e are the initial and equilibrium concentrations of the phosphate solution (mg L^{-1}), respectively; V is the volume of the phosphate solution (L); and m is the weight of the adsorbent (g) which is calculated in section 3.1.3.

The adsorption kinetic experiments were conducted as follows: A piece of ANT was added to 20 mL of the phosphate solution containing 50 mg L^{-1} at three different temperatures (10, 25, and 40°C) with pH adjusted to 5. At regular time intervals (1, 5, 15, 30, 60, 120, 240, and 320 min), liquid samples were withdrawn and analyzed for phosphate concentrations.

The effect of adsorption temperature on phosphate removal was performed at five different temperatures (10, 20, 30, 40, and 50°C) for 4 h with a 20 cm^2-sized piece of ANT at pH 5 and an initial phosphate concentration of 20 mg L^{-1}.

To investigate the effect of pH on adsorption, the initial pH was adjusted to 2.0, 3.0, 4.0, 5.0, 6.0, 7.0, 8.0, 9.0, and 10.0 by adding 0.1M HCl and 0.1M NaOH solutions dropwise. The reaction was monitored for 4 h, and the initial phosphate concentration was fixed at 50 mg L^{-1}.

The point of zero charge (PZC) of ANT was determined using potentiometric titrations [17]. An ANT piece with a size of 20 cm^2 was immersed and shaken in 100 mL of 0.5, 0.05, or 0.005M NaCl electrolyte solution for 30 min. HCl (0.01M) or 0.01M NaOH were used to adjust the pH (3–9) of the electrolyte. The pH_{pzc} was calculated using Eq. (2):

$$\delta_0 = \left(C_A - C_B\right) - \left(H^+ - OH^-\right) \quad (2)$$

where δ_0 = surface charge (mM g^{-1} adsorbent), C_A = acid concentration (mol L^{-1}), C_B = alkali concentration (mol L^{-1}), $H^+ = 10^{-pH}$, and $OH^- = 10^{-(pKw-pH)}$.

The effect of coexisting anions typically present in wastewater, such as Cl^-, HCO_3^-, SO_4^{2-}, and NO_3^-, on the adsorption of phosphate was studied by adding three different concentrations (0.1, 1, 10 mM) of NaCl, $NaHCO_3$, Na_2SO_4, and $NaNO_3$ to 50 mg L^{-1} of the phosphate solution, respectively. The solution pH was adjusted to 5 ± 0.1. An ANT was added to each Falcon tube containing 20 mL of the phosphate solution of concentration 50 mg L^{-1}. After the adsorption equilibrium had been achieved at room temperature, the phosphate concentrations were analyzed. All experiments were replicated for reproducibility, and only the mean values are presented in this paper.

2.5. Desorption of phosphate and reusability of ANT

The reusability of ANT for phosphate recovery was investigated by sequential adsorption and desorption experiments. In each cycle, an ANT was added to 20 mL of a 50 mg L^{-1} phosphate solution for 4 h. After adsorption, the adsorbent was dried and then used for the desorption experiment. The collected adsorbent was added to 20 mL of 5 mM sodium hydroxide solution and shaken at 50 rpm for 4 h. The concentration of the desorbed phosphate was then determined using a spectrophotometer. The adsorption-desorption process was carried out six times to evaluate the reusability of the synthesized ANT for phosphate removal and recovery.

3. Results and discussion

3.1. Characterization

3.1.1. FE-SEM analysis

High-quality ANT arrays having highly oriented nanostructure were fabricated under optimized anodization conditions, i.e., in a 0.3M oxalic acid electrolyte for 8 h at 30 V and 5°C. ANT arrays fabricated via the two-step anodization of Al foil were characterized by FE-SEM, as shown in Figs. 1(a)–(d). The SEM images of the sample after the first anodization step and etching are shown in Figs. 1(a) and (b), respectively. The optimum voltage and time for the first anodization step were 30 V and 8 h, respectively. In Fig. 1(c), the regular and ordered ANT arrays can be clearly observed at the surface of the Al foil. The pore diameter refers to the diameter of the holes made on the ANT, and the wall thickness is the distance between the adjacent pores [23]. The average nanotube diameters and the wall thickness were determined to be approximately 18–22 nm and 100 nm, respectively (Fig. 1(c)). Fig. 1(d) shows a cross-sectional SEM image of the ANT, which proved that ANT was composed of cylindrical and parallel compressed tubes stacked on each other. The average length of the nanotubes was ~10.23 μm. The FE-SEM images of other synthesis conditions are explained and shown in supplementary material Figs. S1–S6.

3.1.2. XRD and EDX analyses

The XRD patterns of pure aluminum and ANT are shown in Fig. 2(a). The diffraction peaks at 2θ values of 65.09° and 78.23° are characteristic of metallic aluminum [24] and those at 38.45° and 44.71° correspond to alumina [25,26]. Interestingly, the XRD peak characteristics of alumina were also observed in the diffraction pattern of the Al foil, which may be a result of the reaction of aluminum with air. After anodization, the intensity of the alumina peaks was increased, which confirmed that alumina had formed on the aluminum substrate surface in the anodizing process. This observation was further confirmed by EDX analysis, as shown in Fig. 2(b). The atomic concentrations of the observed aluminum and oxygen peaks were 48.5% and 51.5%, respectively. The surface functional groups were analyzed using FTIR, and the results were discussed and presented in supplementary material section 1.5 and Fig. S7.

3.1.3. Theoretical mass calculation of synthesized ANT

Unlike the powder type, it is complicated to measure the mass of ANT film produced on the anodized foil. Therefore, Faraday's law can be used to indirectly measure the mass of ANT (g), which is expressed in Eqs. (3)–(5) [27,28].

$$Q = \frac{At}{S} \quad (3)$$

$$L = \frac{QM}{Fn\delta} \quad (4)$$

$$L\delta S = \frac{AtM}{nF} \quad (5)$$

where Q is the charge (C cm^{-2}), M is the molar mass of alumina (101.96 g mol^{-1}), t is the anodization time (s), S is the surface area of Al foil (4 × 5 cm^2), n is the number of electrons, F is the Faraday constant (96,487 C $equiv^{-1}$), L is

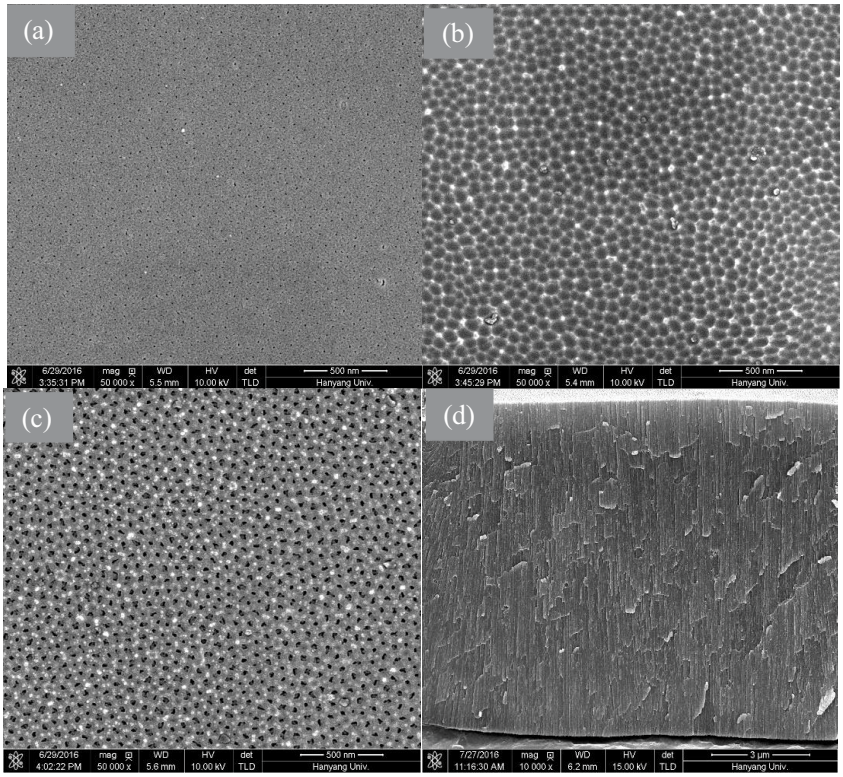

Fig. 1. FE-SEM images of ANT. (a) Top view after first anodization, (b) after etching, (c) after second anodization, and (d) cross-sectional view.

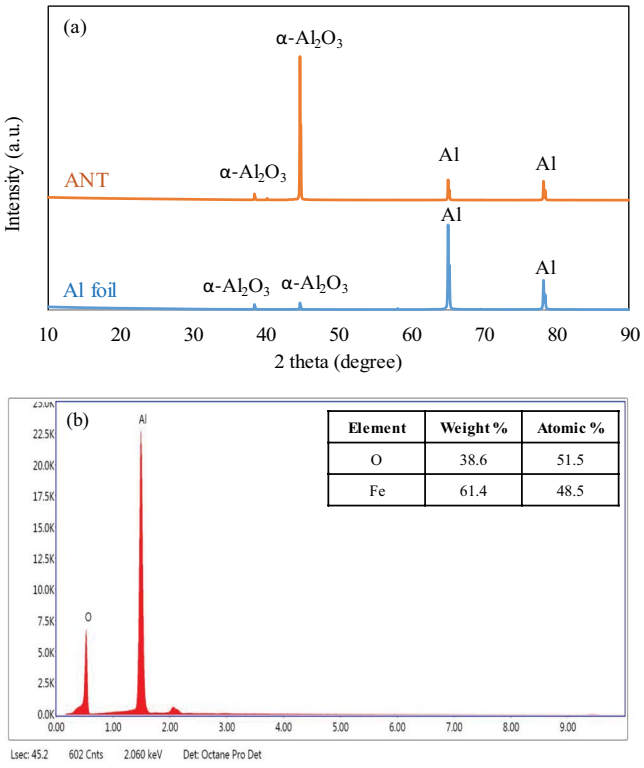

Fig. 2. (a) XRD patterns of Al foil and ANT and (b) EDX analysis of ANT.

the theoretical length of the nanotube, and δ is the density of Al_2O_3 (3.987 g cm^{-3}). The calculated mass of the ANT in this study was about 0.1319 g per foil.

3.2. Adsorption kinetics

A kinetic study of the adsorption process illustrates the relationship between the adsorption rate of the adsorbent and the residence time of the adsorbate at the solution interface. High adsorption rates are as important as a high adsorption capacity to attain satisfactory adsorption performance [29].

The kinetic experiments for phosphate adsorption on ANT were conducted at an initial phosphate concentration of 50 mg L^{-1}. Fig. 3 shows the results of the phosphate adsorption kinetics of ANT at three different temperatures. An equilibrium phosphate adsorption capacity of >89% was achieved by ANT within 1 h. Subsequently, phosphate was adsorbed slowly on the ANT, and the maximum phosphate adsorption was reached after 4 h. Further increase in retention time did not seem to have any effect on the equilibrium concentration. The higher initial adsorption rate may be attributed to an increased number of empty active sites available at the early stages; so, there are increased concentration gradients between the adsorbate in the solution and the adsorbate on the adsorbent surface. The increase in the concentration gradient led to the observed increase in the rate of phosphate adsorption in the early stages. With time, this concentration decreased because of the accumulation of phosphate in the empty sites, and eventually, the sorption rate decreased considerably.

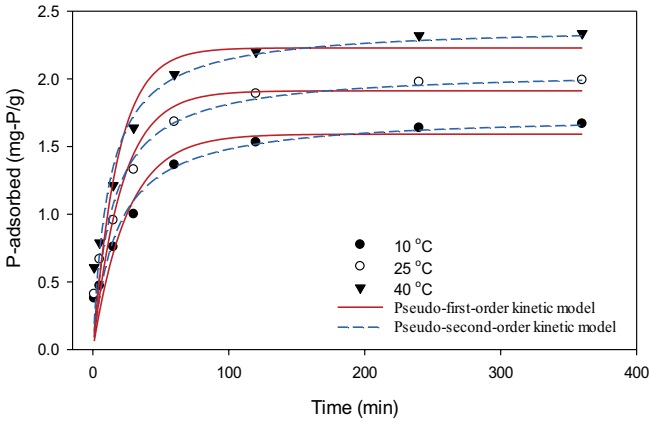

Fig. 3. Adsorption kinetics of phosphorous removal by ANT.

A similar two-step adsorption process of phosphorus on different adsorbents such as magnetite, iron oxide nanotubes (INT), Fe–Mn oxide, aluminum-manganese bimetallic oxide-coated zeolite, and iron-copper binary oxides has been reported in previous studies [30–32]. The adsorption kinetics experimental data were further analyzed using pseudo-first-order and pseudo-second-order kinetic models, which are expressed in Eqs. (6) and (7), respectively.

$$q_t = q_e\left(1 - e^{-k_1 t}\right) \tag{6}$$

$$q_t = \frac{k_2 q_e^2 t}{1 + k_2 q_e t} \tag{7}$$

where q_t is the amount of phosphate (mg g^{-1}) adsorbed on ANT at time t, q_e is the equilibrium adsorption capacity of phosphate (mg g^{-1}), k_1 is the rate constant for the pseudo-first-order reaction (h^{-1}), and k_2 is the rate constant for the pseudo-second-order reaction (g mg^{-1} h^{-1}). Table 1 lists the fitting parameters of phosphate adsorption on ANT using the pseudo-first-order and pseudo-second-order kinetic models. The value of R^2 indicated that the pseudo-second-order kinetic model was a better fit for the obtained data, thus supporting the assumption that the adsorption of phosphate on ANT primarily involved chemisorptions [33,34].

3.3. Effect of pH

Generally, the pH of the solution is an important parameter for controlling the adsorption at the water-adsorbent interface. Many researchers have studied the effect of pH on the adsorption capacity of different adsorbents and have reported that a higher adsorption of phosphorus was achieved at lower pH [35–37]. Based on this result, the adsorption of phosphate per unit weight and the removal efficiency of ANT were studied at different pH values ranging from 2.0 to 10.0, as depicted in Fig. 4(a). It was evident that the adsorption efficiency increased with decreasing pH and reached a maximum (40.8%) at pH 2.0. The adsorption of phosphate on ANT was therefore strongly dependent on pH, and the removal efficiencies were clearly high in acidic media. With an increase in pH up to 10.0, there was a steady decrease in the adsorption efficiency. This may be attributed to the increased competition between the phosphate species

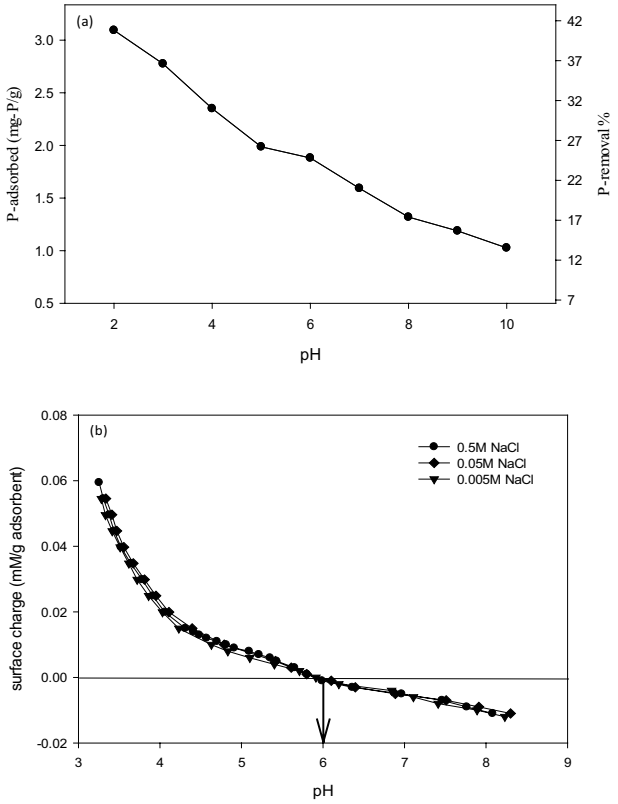

Fig. 4. (a) Effect of pH on the adsorption of phosphate on ANT and (b) point of zero charge (PZC) as a function of ionic strength (conditions: pH was controlled with 0.01M HCl solution and 0.01M NaOH solution, the temperature was 20°C, reaction time was 30 min, and mixing speed was 50 rpm).

Table 1
Kinetic parameters of phosphate adsorption on ANT

Temperature (K)	Pseudo-first-order model			Pseudo-second-order model		
	q_e (mg g^{-1})	k_1 (h^{-1})	R^2	q_e (mg g^{-1})	k_2 (g mg^{-1} h^{-1})	R^2
283	1.59	0.040	0.91	1.74	0.033	0.95
298	1.91	0.047	0.92	2.07	0.035	0.96
313	2.23	0.055	0.89	2.39	0.036	0.94

and the OH^- groups present in the solution for the adsorption sites on ANT. Phosphate can exist as $H_2PO_4^-$, HPO_4^{2-}, and PO_4^{3-} depending on the solution pH with pK_1 = 2.15, pK_2 = 7.20, and pK_3 = 12.33, respectively [38]. A similar trend was also observed for phosphate adsorption on INT, where the amount of phosphate adsorbed on the INTs increased at lower pH and was at a maximum in the pH range 2.0–3.0 [6].

The pH-dependent adsorption capacity of ANT was related to the surface charge of alumina. The PZC of ANT was measured and observed at pH 6 as shown in Fig. 4(b). At pH below the PZC, the surface of ANT was protonated, implying that the surface charge was positive. On the other hand, the surface became deprotonated at pH higher than at PZC. Thus, the decrease in adsorption of phosphate at higher pH is ascribed to an increase in the repulsive forces between the negatively charged phosphate species and surface sites, in addition to the increased competition between the OH^- groups and phosphate species for the adsorption sites.

3.4. Adsorption isotherms

Adsorption isotherms can help explain how the adsorbent interacts with the adsorbate and are important for the determination of the adsorption capacity [39]. In this study, the adsorption characteristics of ANT were investigated by performing a batch isothermal experiment of phosphate adsorption at room temperature, and the results are shown in Fig. 5(a). It was evident from the experimental data that the amount of phosphate adsorbed on ANT increased with the increase in initial phosphate concentration. Langmuir and Freundlich isotherms were used to analyze the phosphate adsorption isotherm data obtained from equilibrium conditions. The basic assumption of the Langmuir isotherm model is that adsorption occurs at a specific site (monolayer adsorption) within the adsorbent, while the Freundlich adsorption isotherm is an empirical equation based on adsorption on a heterogeneous surface that possibly results in multilayer adsorption [40,41]. The Langmuir and Freundlich isotherm models are represented mathematically in Eqs. (8) and (9), respectively.

$$q_e = q_{\max}\frac{K_L C_e}{1 + K_L C_e} \tag{8}$$

$$q_e = K_F C_e^{\frac{1}{n}} \tag{9}$$

where q_e is the amount of adsorbate per unit mass of the adsorbent at equilibrium (mg g^{-1}), $q_{\max}$ (mg g^{-1}) is the maximum adsorption capacity, K_L (L mg^{-1}) is the Langmuir isotherm constant, C_e refers to the equilibrium adsorbate concentration (mg g^{-1}), and K_F (mg g^{-1}) and n are the Freundlich isotherm constants related to the adsorption capacity and adsorption intensity, respectively.

Based on experimental results, it was clear that the Langmuir isotherm model described the phosphate adsorption on ANT more accurately than the Freundlich model. In general, the Langmuir model describes a monolayer adsorption, suggesting that the active sites on the ANT surface have similar adsorption energies. The coefficient of determination (R^2) in the case of the Langmuir model for ANT was relatively higher than that of the Freundlich isotherm model (Table 2). The phosphate adsorption capacity of ANT increased as the temperature increased from 283 to 313 K, suggesting that the adsorption of phosphate was endothermic in nature. The estimated maximum adsorption capacity per unit weight (adsorption density) of ANT using the Langmuir model was 28.1–32.2 mg g^{-1}, while that calculated based on the Freundlich model (K_F) was 0.357–0.740 mg g^{-1}. Table 3 illustrates the comparison of adsorption capacity of ANT with other adsorbents.

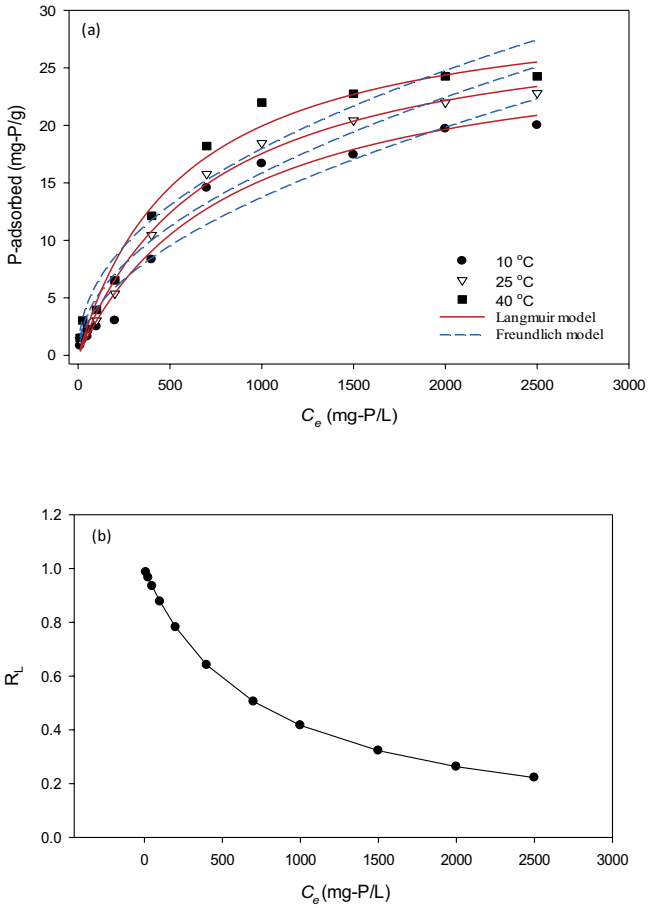

Fig. 5. (a) Adsorption isotherms and (b) plot of separation factor versus initial phosphate concentration.

The fundamental features of the Langmuir model can be illustrated in terms of a dimensionless constant known as the

Table 2
Adsorption isotherm parameters of phosphate on ANT

Temperature (K)	Langmuir isotherm			Freundlich isotherm		
	$q_{\max}$ (mg g^{-1})	K_L (L mg^{-1})	R^2	K_F (mg g^{-1})	$1/n$	R^2
283	28.1	0.0012	0.98	0.357	0.529	0.94
298	30.1	0.0014	0.99	0.497	0.501	0.96
313	32.2	0.0017	0.99	0.740	0.462	0.95

Table 3
Comparison of adsorption capacity of ANT with other adsorbents

S.No	Adsorbent	Experimental conditions				Adsorption capacity (mg g^{-1})	Reference
		C_0 (mg/L)	Temp (°C)	pH	Time (h)		
1	ANT	10–2,500	40	5.0	4	32.2	This study
2	Magnetite	165–1,510	23	7.0	2	15.2	[31]
3	Fe–Mn binary oxide	0.65–13	25	5.6	24	10.8	[54]
4	$NiFe_2O_4$	3.3–32.6	25	3.0	2	13.0	[55]
5	Fe–Mn oxide	3.3–32.6	35	7.0	24	6.0	[46]
6	Al–Fe_3O_4	1–100	–	–	2	33.3	[56]
7	Fe–Cu binary oxide	0.33–8.2	25	5.0	24	13.0	[35]
8	Magnetic Fe–Zr binary oxide	0–100	25	4.0	24	13.6	[57]
9	Iron-doped activated carbon	3.9–14	35	3.8	24	5.0	[58]
10	Al–Mn bimetal oxide-coated zeolite	5–100	25	7.0	24	7.6	[30]
11	NaOH-activated and lanthanum-impregnated zeolite	6.5–163.1	40	7.0	24	3.0	[59]
12	activated aluminum oxide	1.6–65.2	25	6.9	24	6.8	[37]
	lanthanum oxide	1.6–163		9.5		15.3	
13	lanthanum/aluminum-pillared clays	2.5–50	25	5.0	12	13.0	[60]
	Aluminum-pillared clays					10.3	
14	Natural zeolite	3.3–32.6	25	4.0	2	0.4	[51]
	TiO_2/Zeolite	3.3–326.1			0.33	11.3	

separation factor or equilibrium parameter, R_L, which is used to predict if an adsorption system is favorable, as shown in Eq. (10) [42].

$$R_L = \frac{1}{1 + K_L C_0} \tag{10}$$

where C_0 (mg L^{-1}) is the initial phosphate concentration and K_L (L mg^{-1}) is the Langmuir constant. The value of R_L indicates the shape of the isotherms and the nature of the adsorption process as linear (R_L = 1), unfavorable (R_L > 1), favorable (0 < R_L < 1), or irreversible (R_L = 0) [43,44].

The calculated R_L values at different initial phosphate concentrations are shown in Fig. 5(b). The value of R_L was in the range of 0–1, confirming the favorable uptake of phosphate by ANT. Moreover, lower R_L values at higher initial phosphate concentrations indicated that adsorption was more favorable at higher concentrations.

3.5. Thermodynamic parameters

As reported in the literature, the thermodynamic parameters related to the adsorption process can be calculated from the temperature-dependent adsorption isotherms based on Eqs. (11)–(13):

$$K_d = \frac{q_e}{C_e} \tag{11}$$

$$\Delta G^\circ = -RT\ln K_d \tag{12}$$

$$\ln K_d = -\frac{\Delta H^\circ}{RT} + \frac{\Delta S^\circ}{R} \tag{13}$$

where K_d is the distribution coefficient (mL g^{-1}), $\Delta G°$ refers to the Gibbs free energy (kJ mol^{-1}), $\Delta H°$ is the enthalpy (kJ mol^{-1}), $\Delta S°$ is the entropy (kJ mol^{-1} K^{-1}), T is the absolute temperature (K), q_e refers to the equilibrium adsorption capacity per unit weight of the adsorbent (mg g^{-1}), C_e is the equilibrium concentration (mg L^{-1}), and R is the universal gas constant.

The changes in enthalpy ($\Delta H°$) and entropy ($\Delta S°$) were determined from the slope and intercept of a linear plot between $\ln K_d$ and T^{-1}, respectively (Fig. 6). The thermodynamic parameters obtained for the adsorption of phosphate are given in Table 4. The negative values of $\Delta G°$ indicate the spontaneous nature of adsorption [45–47]. The values of $\Delta G°$ for phosphate adsorption on ANT decreased from –11.91 to –18.04 kJ mol^{-1} as the temperature increased from 283 to 323 K, suggesting that the adsorption of phosphate was easier at high temperatures rather than at low temperatures. The positive $\Delta H°$ value (34.54 kJ mol^{-1}) implied that phosphate adsorption on ANT was endothermic, as also evidenced by the increase in the amount of phosphate adsorbed at higher temperatures [48]. Moreover, the positive value of $\Delta S°$ (0.16 kJ mol^{-1}) indicated an increase in the disorder and randomness at the solid-liquid interface during the adsorption of phosphate on ANT.

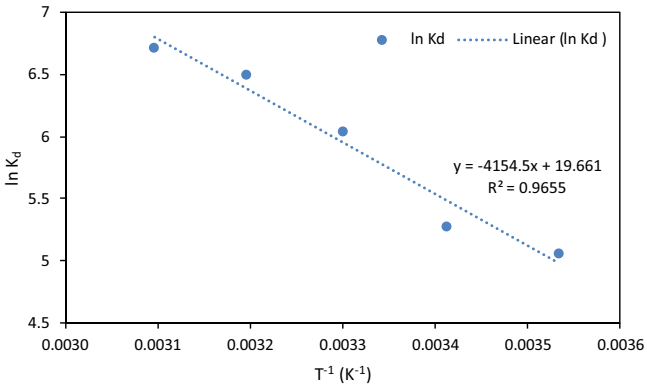

Fig. 6. Plot of lnK_d vs T^{-1} for phosphate adsorption by ANT.

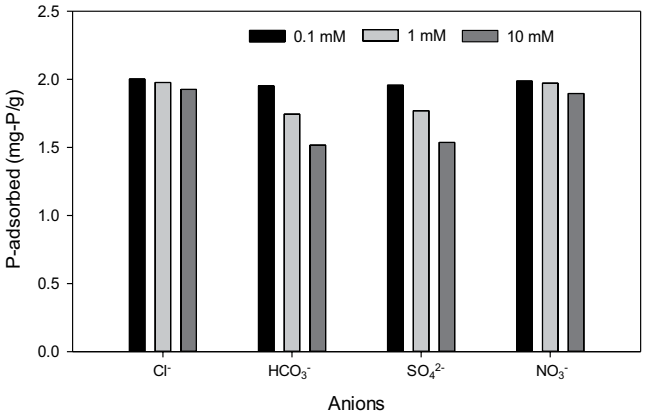

Fig. 7. Effect of coexisting anions on phosphate adsorption at a fixed initial phosphate concentration: 50 mg L^{-1}.

Table 4
Thermodynamic parameters of phosphate adsorption on ANT

T (K)	C_e (mg L^{-1})	q_e (mg g^{-1})	removal %	K_d (mL g^{-1})	$\Delta G°$ (kJ mol^{-1})	$\Delta H°$ (kJ mol^{-1})	$\Delta S°$ (kJ mol^{-1} K^{-1})
283	9.8	1.55	51.0	157.82	–11.91		
293	8.7	1.71	56.5	196.94	–12.87		
303	5.3	2.23	73.5	420.56	–15.22	34.54	0.16
313	3.7	2.47	81.5	667.99	–16.93		
323	3.1	2.56	84.5	826.63	–18.04		

3.6. Effect of coexisting anions

Adsorption selectivity is an important factor influencing the removal efficiency of the absorbent. Some researchers have used highly selective adsorbents to remove or separate heavy metals from aqueous systems [49,50]. However, anions such as chloride, bicarbonate, sulfate, and nitrate are commonly present in wastewater and might interfere with the adsorption of phosphate by competing for the adsorption sites on the adsorbent surface. The effect of these common anions on the adsorption of phosphate at three different concentrations (0.1, 1.0, and 10 mM) was evaluated at pH 5.0 ± 0.1, and the results are shown in Fig. 7.

It was found that the chloride and nitrate anions did not have any obvious effect on phosphate adsorption when their concentrations ranged from 0.1 to 1 mM. However, at a higher concentration of 10 mM of Cl^- and NO_3^-, the adsorption of phosphate decreased by 3.8% and 4.6%, respectively. Therefore, it was concluded that these two anions did not significantly affect phosphate adsorption. However, the coexisting bicarbonate and sulfate anions reduced the phosphate adsorption rate to 76% and 77%, respectively, when the concentration of these anions was increased from 0.1 to 10 mM. The noticeable inhibition because of bicarbonate and sulfate may be a result of the strong competition for the binding sites on the adsorbent between phosphate and these anions. Therefore, the uptake of phosphate by ANT gradually decreased as the concentration of the ions increased.

3.7. Mechanism

Phosphate adsorption mechanism study is of utmost importance to understand the adsorbate-adsorbent interaction. The schematic (Fig. 8) shows a proposed mechanism for adsorption of phosphate on ANT's surface. The phosphate adsorption process depends primarily on electrostatic attraction and chemical interaction [51]. The pH of the phosphate solution plays a significant role in influencing the adsorption process. Generally, as the pH of the solution changes, protonation and deprotonation take place on the adsorbent surface. The phosphate removal process on the surface of ANT can be represented by the following possible reactions (14)–(19) [30]:

$$\mathrm{ANT \equiv OH + H^+ \leftrightarrow ANT \equiv OH_2^+} \quad (14)$$

$$\mathrm{ANT \equiv OH + H_2O \leftrightarrow ANT \equiv OH_2^+ + OH^-} \quad (15)$$

$$\mathrm{ANT \equiv OH \leftrightarrow ANT \equiv O^- + H^-} \quad (16)$$

$$\mathrm{ANT \equiv OH + OH^- \leftrightarrow ANT \equiv O^- + H_2O} \quad (17)$$

$$\mathrm{ANT \equiv OH + H_2PO_4^- \leftrightarrow ANT \equiv H_2PO_4 + OH^-} \quad (18)$$

$$\mathrm{ANT \equiv OH + HPO_4^{2-} \leftrightarrow ANT \equiv HPO_4^- + OH^-} \quad (19)$$

At initial pH < pH_{pzc}, a rise in the final pH of the phosphate solution was observed during adsorption process which could be due to ion exchange of OH^- with phosphate as shown in supplementary material Fig. S7. However, the

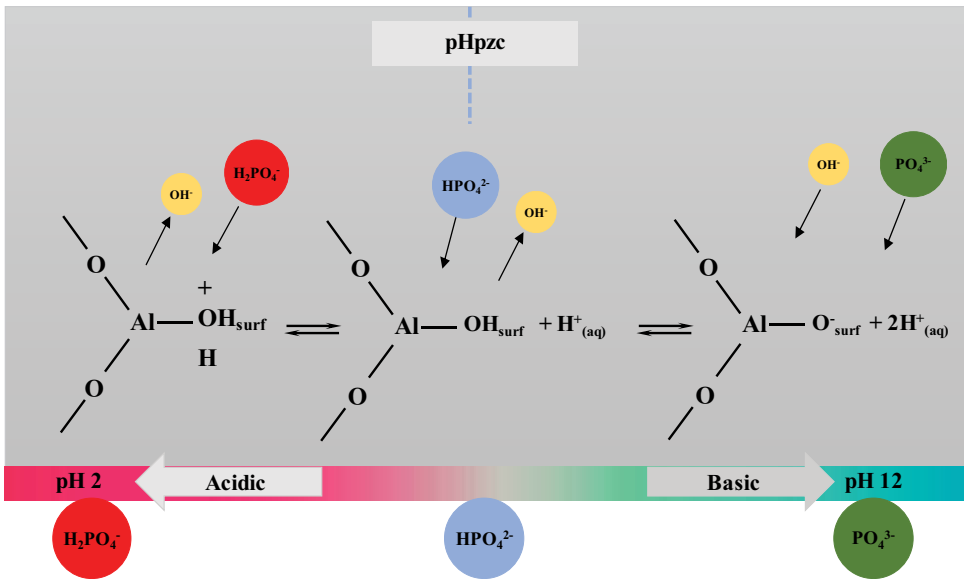

Fig. 8. Phosphate sorption mechanism of ANT.

final pH decreases when the initial pH > pH_{pzc}. The reason could be due to increased adsorption of OH^- group besides phosphate, reducing the concentration of OH^- present in the solution. In general, the main mechanism associated with the adsorption process varies with the pH of the solution. The impacts of electrostatic attraction and ion exchange became weaker while the Lewis acid-base interaction progressively dominated with the rise in pH value [52].

3.8. Desorption and reusability

Regeneration experiments were performed to establish the fundamentals for the mechanism of phosphorus removal from ANT. In addition, these experiments have shown the possible multi-cyclic application of the synthesized adsorbent. It is known that PO_4^{3-} is the predominant species in the solution medium at highly alkaline pH, and the adsorbent is deprotonated and negatively charged, which is suitable for the desorption of the adsorbed phosphate [53]. Typically, NaOH solution is used as an eluent for the desorption of phosphate from used adsorbents, which can then be reused to adsorb phosphate. Therefore, NaOH solution was used for desorption in this study as well. To avoid the risk of damaging the adsorbent, a low concentration of NaOH (5 mM) was used for the desorption of phosphate. The results of six consecutive adsorption-desorption cycles are shown in Fig. 9.

The phosphate adsorption capacity by ANT decreased with respect to the regeneration cycles. The adsorption of phosphate decreased by almost 20% in the second cycle, which might be due to the existence of irreversible adsorption sites on the adsorbent. The phosphate adsorption percentage was 79% in the second cycle and 71%, 67%, 63%, and 67%, in the third, fourth, fifth, and sixth subsequent cycles, respectively. However, the amount of desorbed phosphate increased gradually in the first three cycles and then decreased in the subsequent cycles.

The total amount of phosphate adsorbed and desorbed and the recovery percentage in six regeneration cycles were

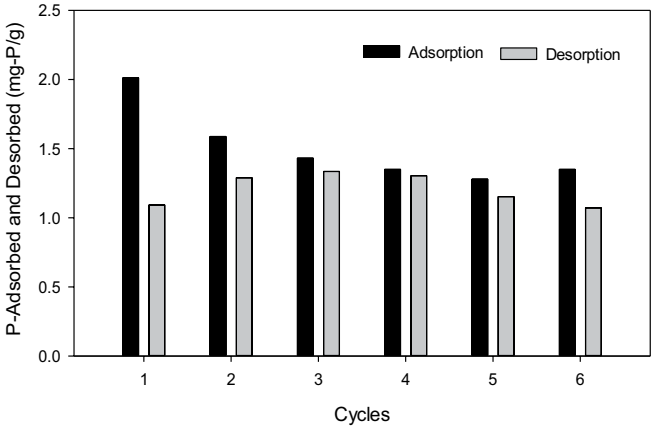

Fig. 9. Variation of the phosphate adsorption capacity on ANT as a function of the regeneration cycle.

9.01 mg g^{-1}, 7.24 mg g^{-1}, and 80.4%, respectively. Therefore, it was concluded that ANT has a great potential for application as a renewable adsorbent.

4. Conclusions

A simple two-step anodization method was proposed for the fabrication of ANT-based nanosorbents for phosphate removal from synthetic wastewater. All experimental conditions were optimized to obtain satisfactory results. The results showed that phosphate can be effectively removed by ANT without pre- and posttreatment of the water samples. The main advantage of the proposed nanosorbents is that they do not require separation of the adsorbent material from the adsorbate solution by filtration. In the adsorption kinetics test, it was found that the pseudo-second-order

model reasonably simulated the adsorption of phosphate on ANT. The adsorption isotherm results illustrated that the Langmuir model was more fitting than the Freundlich model. Thermodynamic studies showed that the adsorption of phosphate on ANT was endothermic and spontaneous. In addition, the adsorption capacity was pH sensitive; the amount of phosphate adsorbed was relatively high at lower pH but decreased linearly with increasing pH. While chloride and nitrate ions had no conspicuous effect on phosphate adsorption, bicarbonate and sulfate had a slight effect when their concentration was increased from 0.1 to 10 mM. The total amount of phosphate adsorbed and desorbed and the recovery percentage were 9.01 mg g^{-1}, 7.24 mg g^{-1}, and 80.4%, respectively.

Acknowledgments

This study was supported by a National Research Foundation of Korea (NRF) grant funded by the Korean Government (grant number NRF-2016R1A2A1A05005388).

References

[1] S. Benyoucef, M. Amrani, Adsorption of phosphate ions onto low cost Aleppo pine adsorbent, Desalination, 275 (2011) 231–236.
[2] S.E. Rosenquist, W.C. Hession, M.J. Eick, D.H. Vaughan, Variability in adsorptive phosphorus removal by structural storm water best management practices, Ecol. Eng., 36 (2010) 664–671.
[3] T.C. Chen, G.-H. Huang, C.-H. Liu, C.-S. Chen, S.-H. Chuang, Y.-H. Huang, Novel effective waste iron oxide-coated magnetic adsorbent for phosphate adsorption, Desal. Wat. Treat., 52 (2014) 766–774.
[4] D. Bhargava, S. Sheldarkar, Effects of adsorbent dose and size on phosphate-removal from wastewaters, Environ. Pollut., 76 (1992) 51–60.
[5] J. Barnard, M. Steichen, Where is biological nutrient removal going now?, Water Sci. Technol., 53 (2006) 155–164.
[6] J. Choi, J. Chung, W. Lee, H.-S. Lim, J.-O. Kim, Recovery of phosphate by magnetic iron oxide particles and iron oxide nanotubes in water, Water Air Soil Pollut., 227 (2016) 1–11.
[7] C. Luedecke, S.W. Hermanowicz, D. Jenkins, Precipitation of ferric phosphate in activated sludge: a chemical model and its verification, Water Sci. Technol., 21 (1989) 325–337.
[8] R.D. Neufeld, G. Thodos, Removal of orthophosphates from aqueous solutions with activated alumina, Environ. Sci. Technol., 3 (1969) 661–667.
[9] J.-Q. Jiang, S. Ashekuzaman, Preparation and evaluation of layered double hydroxides (LDHs) for phosphate removal, Desal. Wat. Treat., 55 (2015) 836–843.
[10] S.I. Pereira, P.M. Castro, Phosphate-solubilizing rhizobacteria enhance Zea mays growth in agricultural P-deficient soils, Ecol. Eng., 73 (2014) 526–535.
[11] A. Oehmen, P.C. Lemos, G. Carvalho, Z. Yuan, J. Keller, L.L. Blackall, M.A. Reis, Advances in enhanced biological phosphorus removal: from micro to macro scale, Water Res., 41 (2007) 2271–2300.
[12] Y. Yao, B. Gao, M. Inyang, A.R. Zimmerman, X. Cao, P. Pullammanappallil, L. Yang, Removal of phosphate from aqueous solution by biochar derived from anaerobically digested sugar beet tailings, J. Hazard. Mater., 190 (2011) 501–507.
[13] M. Zhang, B. Gao, Y. Yao, Y. Xue, M. Inyang, Synthesis of porous MgO-biochar nanocomposites for removal of phosphate and nitrate from aqueous solutions, Chem. Eng. J., 210 (2012) 26–32.
[14] L.E. De-Bashan, Y. Bashan, Recent advances in removing phosphorus from wastewater and its future use as fertilizer (1997–2003), Water Res., 38 (2004) 4222–4246.
[15] N. Mehrabi, M. Soleimani, H. Sharififard, M. Madadi Yeganeh, Optimization of phosphate removal from drinking water with activated carbon using response surface methodology (RSM), Desal. Wat. Treat., 57 (2016) 15613–15618.
[16] X. Cheng, X. Huang, X. Wang, B. Zhao, A. Chen, D. Sun, Phosphate adsorption from sewage sludge filtrate using zinc–aluminum layered double hydroxides, J. Hazard. Mater., 169 (2009) 958–964.
[17] M. Kim, K. Park, J.M. Kim, Phosphate recovery from livestock wastewater using iron oxide nanotubes, Chem. Eng. Res. Design, 114 (2016) 119–128.
[18] W.-Y. Choi, J. Chung, C.-H. Cho, J.-O. Kim, Fabrication and photocatalytic activity of a novel nanostructured TiO_2 metal membrane, Desalination, 279 (2011) 359–366.
[19] I.-D. Kim, A. Rothschild, B.H. Lee, D.Y. Kim, S.M. Jo, H.L. Tuller, Ultrasensitive chemiresistors based on electrospun TiO_2 nanofibers, Nano Lett., 6 (2006) 2009–2013.
[20] H. Masuda, K. Fukuda, Ordered metal nanohole arrays made by a two-step replication of honeycomb structures of anodic alumina, Science, 268 (1995) 1466.
[21] O. Moradlou, S.D. Farashah, F. Masumian, A. Banazadeh, Magnetite nanoplates decorated on anodized aluminum oxide nanofibers as a novel adsorbent for efficient removal of As (III), Int. J. Environ. Sci. Technol., 13 (2016) 1149–1158.
[22] G.E.J. Poinern, N. Ali, D. Fawcett, Progress in nano-engineered anodic aluminum oxide membrane development, Materials, 4 (2011) 487–526.
[23] M.S. Ilango, A. Mutalikdesai, S.K. Ramasesha, Anodization of aluminium using a fast two-step process, J. Chem. Sci., 128 (2016) 153–158.
[24] X.-f. Lei, J.-x. Ma, Synthesis and electrochemical performance of aluminum based composites, J. Braz. Chem. Soc., 21 (2010) 209–213.
[25] Y. Park, D.-S. Park, S.D. Johnson, W.-H. Yoon, B.-D. Hahn, J.-J. Choi, J. Ryu, J.-W. Kim, C. Park, Effect of gas flow rates and nozzle throat width on deposition of α-alumina films of granule spray in vacuum, J. Eur. Ceram. Soc., 37 (2017) 2667–2672.
[26] A.K. Singh, R. Sarkar, Synthesis and characterization of alumina sol and its use as binder in no cement high-alumina refractory castables, Int. J. Appl. Ceram. Technol., 12 (2015) E54–E60.
[27] J.-W. Jang, S.J. Park, J.-W. Park, Quantitative comparison of the photocatalytic efficiency of TiO_2 nanotube film and TiO_2 powder, J. Soil Groundw. Environ., 21 (2016) 8–14.
[28] J.-W. Jang, J.-W. Park, Iron oxide nanotube layer fabricated with electrostatic anodization for heterogeneous Fenton like reaction, J. Hazard. Mater., 273 (2014) 1–6.
[29] M. Li, J. Liu, Y. Xu, G. Qian, Phosphate adsorption on metal oxides and metal hydroxides: a comparative review, Environ. Rev., 24 (2016) 319–332.
[30] T. Liu, B. Chang, K. Wu, The performance of phosphate removal using aluminium-manganese bimetal oxide coated zeolite: batch and dynamic adsorption studies, Desal. Wat. Treat., 57 (2016) 4220–4233.
[31] J. Choi, J. Chung, W. Lee, J.-O. Kim, Phosphorous adsorption on synthesized magnetite in wastewater, J. Ind. Eng. Chem., 34 (2016) 198–203.
[32] J. Chung, J. Choi, H.-S. Lim, J.-O. Kim, Recovery of phosphate from aqueous solutions using self-organized iron oxide nanotubes, Sci. Adv. Mater., 8 (2016) 1728–1736.
[33] E. Zong, D. Wei, H. Wan, S. Zheng, Z. Xu, D. Zhu, Adsorptive removal of phosphate ions from aqueous solution using zirconia-functionalized graphite oxide, Chem. Eng. J., 221 (2013) 193–203.
[34] Y.-S. Ho, G. McKay, Pseudo-second order model for sorption processes, Process Biochem., 34 (1999) 451–465.
[35] G. Li, S. Gao, G. Zhang, X. Zhang, Enhanced adsorption of phosphate from aqueous solution by nanostructured iron (III)–copper (II) binary oxides, Chem. Eng. J., 235 (2014) 124–131.
[36] W. Xie, Q. Wang, H. Ma, H. Ogawa, Phosphate removal from wastewater using aluminium oxide as adsorbent, Int. J. Environ. Pollut., 23 (2005) 486–491.

[37] J. Xie, Y. Lin, C. Li, D. Wu, H. Kong, Removal and recovery of phosphate from water by activated aluminum oxide and lanthanum oxide, Powder Technol., 269 (2015) 351–357.
[38] J. Das, B. Patra, N. Baliarsingh, K. Parida, Adsorption of phosphate by layered double hydroxides in aqueous solutions, Appl. Clay Sci., 32 (2006) 252–260.
[39] D. Southam, T. Lewis, A. McFarlane, J. Johnston, Amorphous calcium silicate as a chemisorbent for phosphate, Curr. Appl. Phys., 4 (2004) 355–358.
[40] S.T. Akar, A.S. Özcan, T. Akar, A. Özcan, Z. Kaynak, Biosorption of a reactive textile dye from aqueous solutions utilizing an agro-waste, Desalination, 249 (2009) 757–761.
[41] C. Namasivayam, D. Sangeetha, Equilibrium and kinetic studies of adsorption of phosphate onto $ZnCl_2$ activated coir pith carbon, J. Colloid Interface. Sci., 280 (2004) 359–365.
[42] B. Meroufel, O. Benali, M. Benyahia, Y. Benmoussa, M. Zenasni, Adsorptive removal of anionic dye from aqueous solutions by Algerian kaolin: characteristics, isotherm, kinetic and thermodynamic studies, J. Mater. Environ. Sci., 4 (2013) 482–491.
[43] E. Igberase, P. Osifo, A. Ofomaja, Adsorption of metal ions by microwave assisted grafting of cross-linked chitosan beads. Equilibrium, isotherm, thermodynamic and desorption studies, Appl. Organomet. Chem., 32 (2018) e4131.
[44] Z. Wang, D. Shen, F. Shen, T. Li, Phosphate adsorption on lanthanum loaded biochar, Chemosphere, 150 (2016) 1–7.
[45] M. Pan, X. Lin, J. Xie, X. Huang, Kinetic, equilibrium and thermodynamic studies for phosphate adsorption on aluminum hydroxide modified palygorskite nano-composites, RSC Adv, 7 (2017) 4492–4500.
[46] X. Du, Q. Han, J. Li, H. Li, The behavior of phosphate adsorption and its reactions on the surfaces of Fe–Mn oxide adsorbent, J. Taiwan Inst. Chem. Eng., 76 (2017) 167–175.
[47] J.-W. Son, J.-H. Kim, J.-K. Kang, S.-B. Kim, J.-A. Park, C.-G. Lee, J.-W. Choi, S.-H. Lee, Analysis of phosphate removal from aqueous solutions by hydrocalumite, Desal. Wat. Treat., 57 (2016) 21476–21486.
[48] A. Ivanets, V. Srivastava, N. Kitikova, I. Shashkova, M. Sillanpää, Kinetic and thermodynamic studies of the Co (II) and Ni (II) ions removal from aqueous solutions by Ca-Mg phosphates, Chemosphere, 171 (2017) 348–354.
[49] X. Chen, K.F. Lam, S.F. Mak, K.L. Yeung, Precious metal recovery by selective adsorption using biosorbents, J. Hazard. Mater., 186 (2011) 902–910.
[50] X. Chen, K.F. Lam, K.L. Yeung, Selective removal of chromium from different aqueous systems using magnetic MCM-41 nanosorbents, Chem. Eng. J., 172 (2011) 728–734.
[51] A. Alshameri, C. Yan, X. Lei, Enhancement of phosphate removal from water by TiO2/Yemeni natural zeolite: preparation, characterization and thermodynamic, Microporous Mesoporous Mater., 196 (2014) 145–157.
[52] J. Liu, L. Wan, L. Zhang, Q. Zhou, Effect of pH, ionic strength, and temperature on the phosphate adsorption onto lanthanum-doped activated carbon fiber, J. Colloid Interface. Sci., 364 (2011) 490–496.
[53] L. Cumbal, A.K. SenGupta, Arsenic removal using polymer-supported hydrated iron (III) oxide nanoparticles: role of Donnan membrane effect, Environ. Sci. Technol., 39 (2005) 6508–6515.
[54] G. Zhang, H. Liu, R. Liu, J. Qu, Removal of phosphate from water by a Fe–Mn binary oxide adsorbent, J. Colloid Interface. Sci., 335 (2009) 168–174.
[55] Z. Jia, Q. Wang, J. Liu, L. Xu, R. Zhu, Effective removal of phosphate from aqueous solution using mesoporous rodlike $NiFe_2O_4$ as magnetically separable adsorbent, Colloids Surf A Physicochem. Eng. Asp., 436 (2013) 495–503.
[56] J. Xu, L. Luu, Y. Tang, Phosphate removal using aluminum-doped magnetic nanoparticles, Desal. Wat. Treat., 58 (2017) 239–248.
[57] F. Long, J.-L. Gong, G.-M. Zeng, L. Chen, X.-Y. Wang, J.-H. Deng, Q.-Y. Niu, H.-Y. Zhang, X.-R. Zhang, Removal of phosphate from aqueous solution by magnetic Fe–Zr binary oxide, Chem. Eng. J., 171 (2011) 448–455.
[58] Z. Wang, E. Nie, J. Li, M. Yang, Y. Zhao, X. Luo, Z. Zheng, Equilibrium and kinetics of adsorption of phosphate onto iron-doped activated carbon, Environ. Sci. Pollut. Res., 19 (2012) 2908–2917.
[59] Y. He, H. Lin, Y. Dong, Q. Liu, L. Wang, Simultaneous removal of ammonium and phosphate by alkaline-activated and lanthanum-impregnated zeolite, Chemosphere, 164 (2016) 387–395.
[60] S. Tian, P. Jiang, P. Ning, Y. Su, Enhanced adsorption removal of phosphate from water by mixed lanthanum/aluminum pillared montmorillonite, Chem. Eng. J., 151 (2009) 141–148.

Supplementary Information

Table S1
Synthesis conditions of ANT using anodization method

#	Pretreatment	First anodization			Etching	Second anodization		
		Electrolyte	Voltage (V)	Time (h)		Electrolyte	Voltage (V)	Time (h)
1	Ultrasonic cleaning acetone 15 min	Oxalic acid (0.3M)	10	4	H_3PO_4 + H_2CrO_4 (6 wt.% + 1.8 wt.%) Time = 4 h Temperture = 60°C	Oxalic acid (0.3M)	–	–
2			20					
3			30					
4			40					
5			50					
6			60					
7			70					
8	Electropolishing ethanol: $HClO_4$ = 4:1 (v/v), 10 V, 5 °C, 3 min			1				
9				2				
10				3				
11				4				
12				5				
13				6				
14				7				
15			30	8				
16	Annealing 20 min, 500 °C			8			30	1
17								2
18								3
19								4
20								5
21								6
22								7
23								8

1. Field emission scanning electron microscopy

1.1. Effect of voltage on first anodization

To find the optimum voltage for the synthesis of ANT, first anodization was carried out in 0.3M oxalic acid at different potentials in the range of 10–70 V (fixed at 4 h) as shown in Figs. S1(a)–(g). As compared with others, the FE-SEM image shown in Fig. S1(c) illustrates that pores of uniform size were formed during anodization at 30 V. It can be observed from other FE-SEM images of Fig. S1 that the variations in the pore size were increased as the voltage increased. Therefore, 30 V was used as the optimum voltage for the synthesis of ANT.

1.2. Effect of time on first anodization

The first anodization was also performed at different time intervals of 1–8 h at a fixed voltage of 30 V, as shown in Figs. S2(a)–(g). Increasing the anodization time (up to 8 h) leads to the formation of more clear pores. Further increase not uniform. Therefore, to synthesize regular and uniform nanotubes, the alumina formed during the first anodization process was removed with an etching solution, providing a basis for forming regular, ordered, and uniform nanotubes during the second anodization process.

1.3. Effect of time on second anodization

The SEM images of the second anodization process carried out at different time intervals of 1–8 h (fixed at 30 V) are shown in Figs. S3(a)–(e). Fig. S3(e) at 8 h shows a more uniform and regular nanotube formation. Longer anodization time gave longer and more uniform nanotube formation, as shown in FE-SEM cross view (Figs. S4(a)–(e) and S5).

1.4. Effect of second anodization time on phosphate removal efficiency

Phosphate removal efficiency also increases with increasing second anodization time (fixed at 30 V) as shown in Fig. S6.

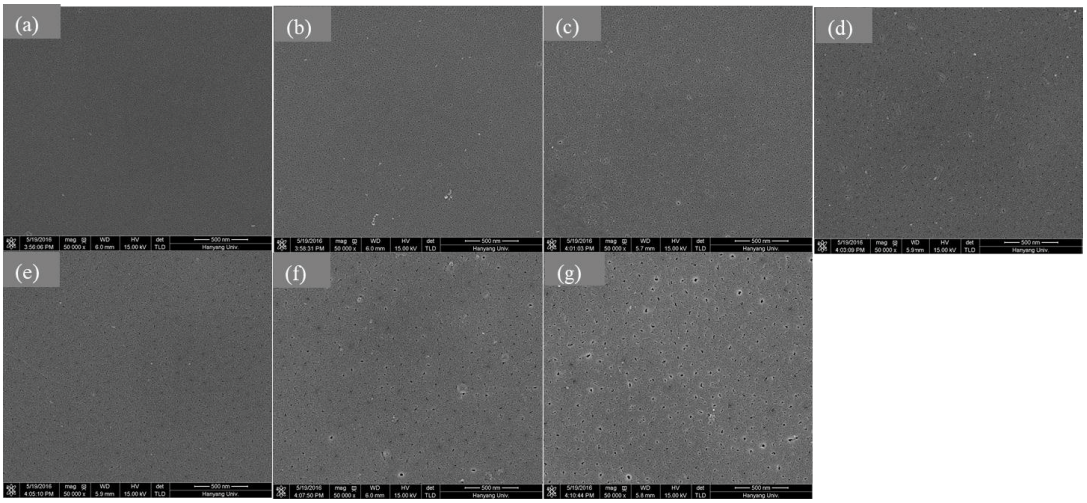

Fig. S1. FE-SEM images for the effect of voltage on first anodization (time fixed at 4 h): (a) 10 V, (b) 20 V, (c) 30 V, (d) 40 V, (e) 50 V, (f) 60 V, and (g) 70 V.

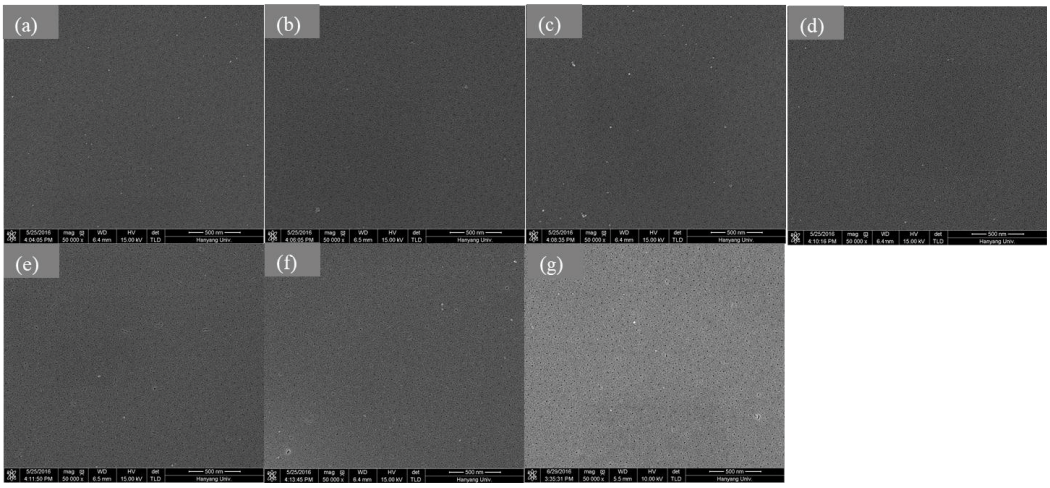

Fig. S2. FE-SEM images of first anodization at fixed 30 V and different times: (a) 1 h, (b) 2 h, (c) 3 h, (d) 5 h, (e) 6 h, (f) 7 h, and (g) 8 h.

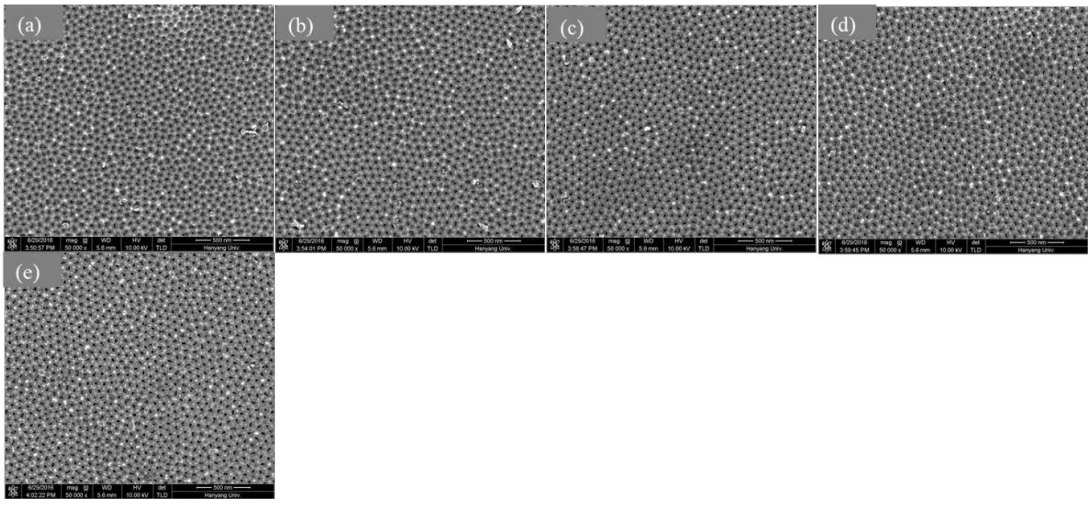

Fig. S3. FE-SEM images of second anodization at fixed 30 V and different times: (a) 1 h, (b) 2 h, (c) 4 h, (d) 6 h, and (e) 8 h.

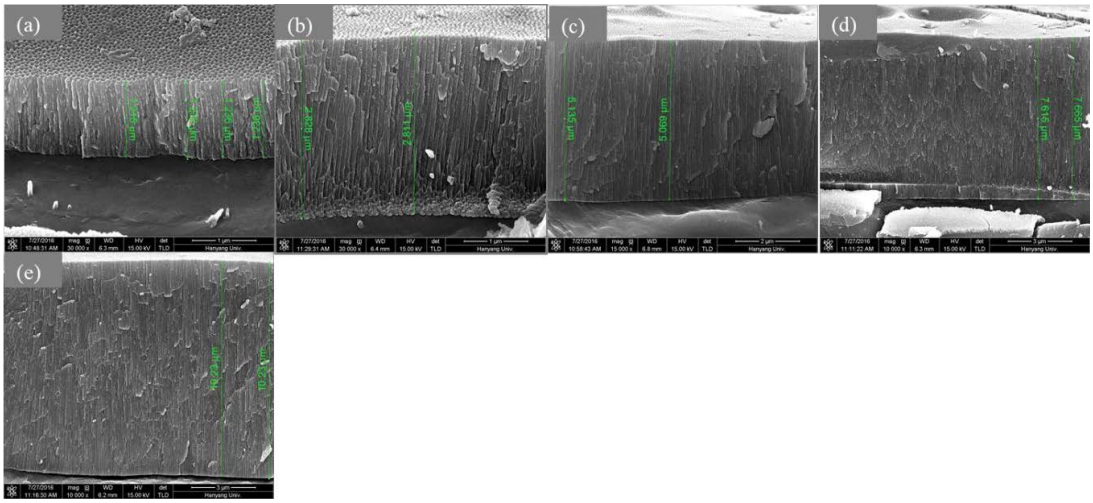

Fig. S4. Cross view FE-SEM images of second anodization at fixed 30 V and different times: (a) 1 h, (b) 2 h, (c) 4 h, (d) 6 h, and (e) 8 h.

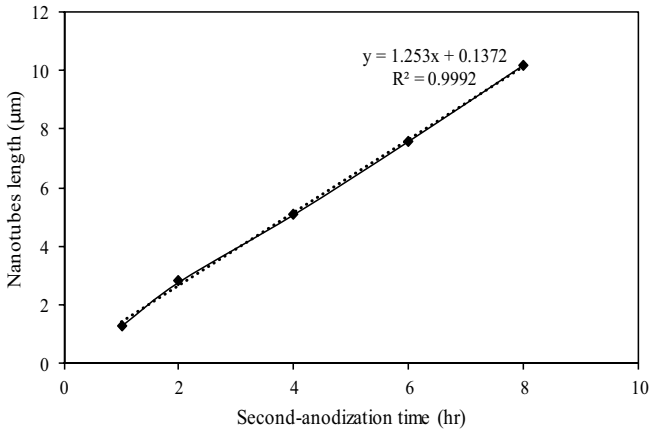

Fig. S5. Plot of nanotube length vs second anodization time (fixed at 30 V).

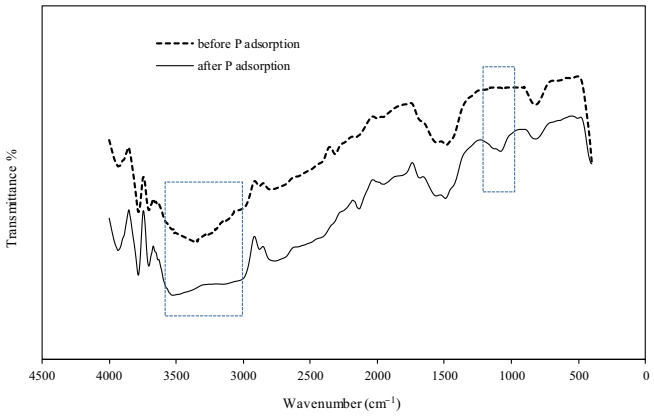

Fig. S7. FTIR analysis of ANT before and after phosphate adsorption.

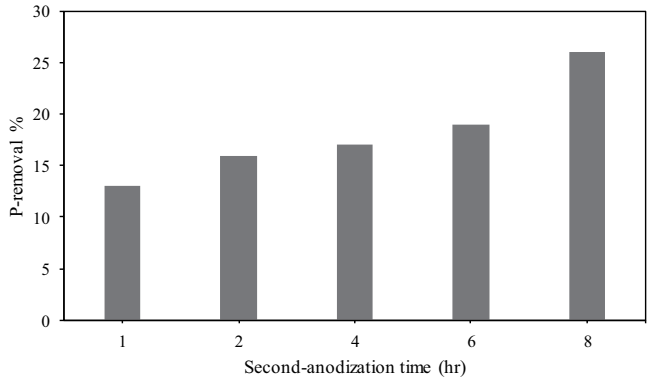

Fig. S6. Effect of second anodization time on phosphate removal efficiency (initial phosphate concentration 50 mg L^{-1}, pH 5, and adsorption time 4 h).

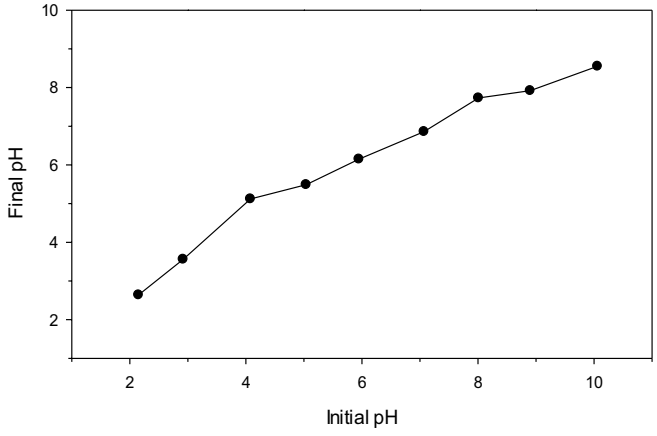

Fig. S8. pH evolution of the solution during adsorption experiment.

2. Fourier transform infrared spectroscopy

FTIR spectra of ANT before and after phosphate adsorption experiment are shown in Fig. S7. The numerous peaks show that ANTs are highly enriched with functional groups. Such highly functional surface is essential for faster adsorption at high phosphate content. The major difference between before and after phosphate adsorption by ANT is in two peaks of FTIR. Whereas, an additional peak at 1,050 cm^{-1} could be referred to PO vibration, and the change in shape of broad –OH peak refers that the –OH groups are playing a significant role in the adsorption of phosphate.

3. pH evolution during adsorption experiment

Fig. S8 shows the pH evolution of the solution during adsorption. The initial pH was adjusted to 2.0, 3.0, 4.0, 5.0, 6.0, 7.0, 8.0, 9.0, and 10.0 by dropwise addition of 0.1M HCl and 0.1M NaOH solutions. The reaction was monitored for 4 h, and the initial phosphate concentration was fixed at 50 mg L^{-1}. At pH < 7, the final pH of the solution raised; however, at pH > 7, the final pH decreased as shown in Fig. S8.